Towards Time Ordered Parton Showers

André Cordeiro
Instituto Superior Téncico — Physics Department
(Dated: October 2021)

Ultra-relativistic heavy ion collisions, such as those at the Large Hadron Collider (LHC) and Relativistic Heavy-Ion Collider (RHIC) have unlocked the study of a hot dense state of matter known as the Quark-Gluon Plasma (QGP), whose dynamics can be accessed by examining the substructure of jets — collimated sprays of particles produced in the collision.

In this context, we introduced the τ jet reclustering algorithm, defined such that its distance measure coincides with the inverse splitting formation time τ_{form}^{-1} in the soft collinear limit. By clustering jets in this way, the τ algorithm is shown to accurately estimate τ_{form} for event samples in Monte Carlo event generators. Further, jet populations can be selected according to their medium modifications.

These results motivate the need for a parton shower ordered according to splitting formation time, a prescription thus far absent from jet studies. To this end, the QCD amplitude for double gluon emission is examined, so that τ_{form} can be computed from an analytical expression, and factorisation into single gluon emissions can be verified.

Lastly, three different prescriptions for parton showers in the *double logarithmic approximation* (DLA) were implemented, corresponding to ordering parton emissions in virtuality, transverse momentum, or splitting angle. The Lund plane distributions for parton cascades in each prescription were obtained, their trajectories over the phase space were investigated, and the τ_{form} values were extracted. The variations between all three prescriptions may prove crucial for QGP studies, highlighting the need for theoretical control beyond the DLA.

I. INTRODUCTION

A. Quantum Chromodynamics

The dynamics of quarks and gluons are described by an SU(3) gauge theory known as Quantum Chromodynamics (QCD), and encoded in the following Lagrangian,

$$\begin{aligned} \mathscr{L}_{\mathsf{classical}} &= \overline{\psi}(\mathrm{i}\not{D} - \mathsf{M})\psi - \frac{1}{4}F^a_{\mu\nu}F^{a,\mu\nu}\,, \\ D_\mu &= \partial_\mu - \mathrm{i}\,g\,\mathsf{T}^a\,A^a_\mu\,, \\ F^a_{\mu\nu} &= \partial_\mu A^a_\nu - \partial_\nu A^a_\mu + g\,f^{abc}\,A^b_\mu\,A^c_\nu\,. \end{aligned} \tag{1}$$

Here, the fields ψ, $\overline{\psi}$, and A^a_μ represent the quark, antiquark, and gluon degrees of freedom respectively. D_μ represents the covariant derivative, defined from the SU(3) generators T^a, and $F^a_{\mu\nu}$ is the field strength tensor, requiring the SU(3) structure constants f^{abc}. Overviews of quantum chromodynamics can be found in [1, 2].

Although the quark, antiquark, and gluon fields described above are appropriate degrees of freedom at high energy scales, the observed particles of the theory are hadrons, which become the appropriate object at low energy scales. This separation between short and long range scales gives rise to the problem of relating calculations in perturbation theory with the non-perturbative objects in the initial and final states of any given experiment.

B. Factorisation of Hard Processes and Parton Evolution

High-energy interactions between hadrons can be factorised into long range, non-perturbative contributions containing all information about the hadron structure, and a short range, perturbative contribution encoding the interaction between constituent partons.

As an example, the cross-section for a proton-proton (pp) scattering with at least one final state hadron can be written as

$$\begin{aligned} \mathrm{d}\sigma_{p+p'\to h+Y} = \sum_{a,b,c}\int_{x_a,x_b} & f_{a/p}(x_a,\mu^2) f_{b/p'}(x_b,\mu^2)\times \\ & \times \mathrm{d}\sigma_{a+b\to c}(x_a,x_b,\mu^2)\times \\ & \times D_{h/c}(x_h,\mu^2)\,. \end{aligned} \tag{2}$$

The first two objects are parton distribution functions (PDFs), $f_{i/p}(x_i,\mu^2)$, which encode the probability of finding a parton i inside hadron p, at a given resolution scale μ^2 and with a momentum fraction of the incoming hadron x_i. Next, the hard scattering cross-section $\mathrm{d}\sigma_{a+b\to c}$ encodes the probability of the scattering between partons a and b to produce parton c (along with any other products). Finally, the fragmentation function (FF) $D_{h/c}(x_h,\mu^2)$ represents the probability of hadron h being produced with a momentum fraction x_h from a parton species c, at some scale μ^2.

Worth noting is that of these objects, only the hard scattering cross-section is calculable in perturbation theory. As such, the PDFs and FFs can only be determined from experiments, see [3, 4].

Despite being non-perturbative, the fragmentation functions and parton distributions evolve perturbatively with the resolution scale μ^2. In fact, a change in the fragmentation functions due to a decrease resolution scale $\mu^2 \to \mu^2 + \delta\mu^2$ is understood as due to partons leaving or entering the $[\mu^2, \mu^2+\delta\mu^2]$ region.

This gives rise to the DGLAP equations,

$$\frac{\mathrm{d}D_a(x,\mu^2)}{\mathrm{d}\ln(\mu^2)} = \frac{\alpha(\mu^2)}{2\pi}\sum_i\int_x^1 \mathrm{d}z\,\frac{D_i(x/z)}{z}\,P_{a\leftarrow i}(z)\,, \tag{3}$$

describing the change in fragmentation functions with

the hardness scale μ^2. The $P_{a\leftarrow i}(z)$ functions are known as the *splitting kernels*, and encode the probability for a parton of species i to produce a parton of species a, carrying some fraction z of its momentum.

This description allows for a probabilistic sampling of a parton cascade, as long as one can compute the probability distribution for the splitting scales. This is given by the Sudakov form factor,

$$\Delta_a(Q_0^2, Q^2) = \\ = \exp\left[-\int_{Q_0^2}^{Q^2} \frac{\mathrm{d}\mu^2}{\mu^2} \frac{\alpha(\mu^2)}{2\pi} \int_{z_{\min}}^{z_{\max}} \mathrm{d}z \sum_i \hat{P}_{i\leftarrow a}(z) \right], \quad (4)$$

defined by the probability for no emission by a parton of species a between the scales $[Q_0^2, Q^2]$.

By sampling the Sudakov form factor, as well as the splitting kernels, one is able to correctly generate the emission scales μ_n^2 and momentum fractions z_n corresponding to a parton cascade and, from momentum conservation, extract the four-momenta of all participating particles. Notably, the integrand in the Sudakov factor depends on the phase space measure $\mathrm{d}\ln\mu^2\,\mathrm{d}z$, invariant under some change of variable to a different scale $\rho^2 = \mu^2 f(z)$, since

$$\mathrm{d}\ln\rho^2 \mathrm{d}z = \det \begin{bmatrix} 1 & f'(z)/f(z) \\ 0 & 1 \end{bmatrix} \mathrm{d}\ln\mu^2 \mathrm{d}z = \\ = \mathrm{d}\ln\mu^2 \mathrm{d}z. \quad (5)$$

Thus, within the *leading logarithmic approximation*, one may take the ordering variable to by a proxy for a kinematic variable of choice, such as the transverse momentum or the splitting angle of the splitting, without compromising the emission probabilities. However, these prescriptions differ in the form of the available phase-space for the emissions.

One such ordering variable is the *splitting angle*, reflecting the angular ordering property of QCD emissions, as outlined in [1, p.182], wherein splitting angles are strictly decreasing along a final state parton cascade. This can be understood as a coherence effect: for angles larger than the antenna's opening, its constituents cannot be resolved by the gluon as individual emitters and therefore act as colour singlet, which does not radiate.

C. Jet Reconstruction Algorithms

A complete experimental treatment of multiple QCD emissions requires a systematic procedure to extract information from the final state particles reaching the detectors, formed by the hadronisation of the final partons. To this end, hadrons are reconstructed as a jet — a collimated spray of final state particles.

This is achieved by sequential reconstruction algorithms such as those of the *generalised-k_T* family, which clusters pairs of particles with minimal distance d_{ij}, until all distances exceed the beam distance d_{iB}, as defined below,

$$d_{ij} \overset{\text{def}}{=} \min(p_{\mathsf{T}i}^{2p}, p_{\mathsf{T}j}^{2p}) \left(\frac{\Delta R_{ij}}{R} \right)^2, \\ d_{iB} \overset{\text{def}}{=} p_{\mathsf{T}i}^{2p}, \quad (6) \\ \Delta R_{ij} \overset{\text{def}}{=} \sqrt{(\varphi_i - \varphi_j)^2 + (y_i - y_j)^2}.$$

Here, ΔR_{ij} represents the geometric distance in the azimuthal angle — rapidity plane, and p regulates the energy dependence of the clustering distance d_{ij}.

Setting $p = -1$ defines the anti-$\mathrm{k_T}$ algorithm, which prioritises splittings with at least one high-energy particle, and is therefore much more likely to identify products of the hard-scattering. This decreased sensitivity to the underlying event along with the fact it produces circular jets means that this algorithm is particularly suited for experimental use. However, due to its tendency to include hard partons in every splitting, the substructure of anti-$\mathrm{k_T}$ ordered jets does not respect the orderings suggested by perturbative QCD calculations.

On the other hand, $p = 0$ defines the Cambridge-Aachen (C/A) algorithm which clusters particles according to their angular distance, yielding jets ordered such that splittings are strictly decreasing in angle. Despite respecting the angular ordering prescription of QCD, its lack of a p_{T} dependence renders it overly sensitive to wide and soft emissions, like those constituting the underlying event.

D. The Quark-Gluon Plasma and Heavy Ions

In ultra-relativistic heavy-ion collisions, such as those studied at RHIC in the Brookhaven National Laboratory, and at the LHC in CERN, a hot dense state of QCD matter known as the quark-gluon plasma (QGP) is formed. Among its many interesting properties, the QGP exhibits deconfinement of the parton degrees of freedom, due to the asymptotic freedom exhibited by QCD at high energies.

Owing to its extreme temperature and density, the QGP expands rapidly, with a short lifetime, in the yoctosecond scale ($10^{-24}\,\mathrm{s}$), and therefore can only be studied indirectly, with recourse to probes defined from products of the hadron collision. Of these, the most relevant to this work are jets, due to containing information about QCD splittings at scales ranging from the hard scattering ($\sim 1\,\mathrm{TeV}$ at the LHC) to the hadronisation scale ($\sim 10^2\mathrm{MeV}$). Thus, the jet modifications due to medium interactions, generally denoted by *jet quenching*, encode the information of the medium evolution across all these energy scales, which can be translated into time scales [5].

In this work, we aim at a more precise determination of the characteristic timescales for parton emissions, in order to eventually unlock precision QGP studies.

II. JET RECONSTRUCTION AND HEAVY ION STUDIES

A. Formation Time and Jet Reconstruction

In cases where parton cascades evolve alongside a deconfined medium, as in heavy ion collisions, the angular ordering prescription for parton showers no longer suffices, and the phase-space for possible emissions opens up to anti-angular ordered showers [6, 7]. Therefore, a reclustering algorithm using a purely geometric distance, such as Cambridge-Aachen, may not provide a suitable jet definition for jet quenching studies.

As the dynamics of all medium properties depend on the medium evolution, the QGP provides a *time direction* for the subsequent evolution of parton cascades. As such, in this section, consisting of work published in [8], we introduce a jet reclustering algorithm ordered in splitting formation time, and explore an application to heavy-ion studies.

To this end, we shall consider the splitting of an off-shell parton with four-momentum p into two daughters with four-momenta p_1 and p_2, as depicted in figure 1.

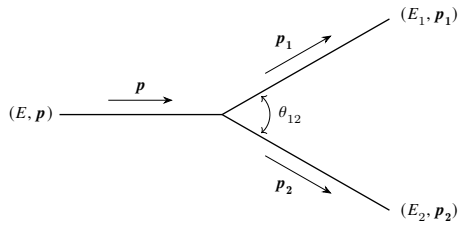

FIG. 1: Kinematics of a $1 \to 2$ parton splitting. The angle between the daughters' three-momenta is denoted θ_{12}.

In the mother's rest frame, and by dimensional analysis, the formation time of such a splitting is inversely proportional to the only mass scale, given by the off-shell mass $m^2 = p^2$. By applying a boost into an the laboratory frame, one finds

$$\tau_{\text{form}} = \frac{E}{m} \cdot \frac{1}{m} \,. \tag{7}$$

This estimation, based on dimensional analysis [2], provides our definition of the timescale of a parton splitting for the rest of this section. By defining z as the energy fraction of the softest daughter and the daughter masses as m_1 and m_2 respectively, the formation time is

$$\begin{aligned} \tau_{\text{form}} &= \frac{E}{m_1^2 + m_2^2 + 2\,p_1 \cdot p_2} \\ &\sim \frac{E}{2\,E_1\,E_2\,(1-\cos\theta_{12})} \\ &\sim \frac{1}{2\,E\,z(1-z)\,(1-\cos\theta_{12})} \\ &\sim \frac{1}{E\,z\,\theta_{12}^2} \,, \end{aligned} \tag{8}$$

noting the assumption of massless daughters in the second line, followed by the soft ($z \ll 1$) and collinear ($\theta_{12} \ll 1$) limit in the third line.

In collider experiments, the momentum component transverse to the beamline (p_{T}) is usually taken as a proxy for the energy, and in central regions of the detector the opening angle can be computed as the distance in the $y - \varphi$ (rapidity – azimuth) plane, given by $\Delta R_{ij}^2 \overset{\text{def}}{=} (\varphi_i - \varphi_j)^2 + (y_i - y_j)^2$. Therefore, using the collider kinematics for the daughter particles $(p_{\text{T}1,2}, \varphi_{1,2}, y_{1,2})$, we can define a proxy for the formation time,

$$\tau_{\text{form}}^{-1} \sim \min(p_{\text{T}1}, p_{\text{T}2})\,(\Delta R_{12})^2 \propto d_{12} \,, \tag{9}$$

where d_{12} represents the generalised-k_T distance between the daughters, with the algorithm exponent $p = 1/2$. Thus, our estimate suggests that this algorithm, hereon denoted the τ *algorithm*, clusters jets ordered in splitting formation time, in the soft collinear limit.

B. Methodology

In order to evaluate the performance of the generalised-k_T algorithms we will use three event generators with different choices of ordering variable. PYTHIA8 [9] (v8.2.35, tune 4C), uses transverse momentum as an ordering variable, and will be used as a reference for vacuum propagated parton cascades. JEWEL (unofficial version based on v.2.2.0) [10], which uses the virtual mass as the ordering variable, will be used as a vacuum reference for jet quenching. Finally, the medium model implemented in JEWEL, which uses a veto in formation time, is used for jet quenching studies.

The event generators were set to produce dijet events at a centre-of-mass energy $\sqrt{s_{\text{NN}}} = 5.02\,\text{TeV}$. The medium effects are implemented in JEWEL through a toy model of an ideal quark-gluon gas, expanding according to a Bjorken model with $T_{\text{init}} = 0.44\,\text{GeV}$ and $\tau_{\text{init}} = 0.4\,\text{fm/c}$.

C. Reclustering Scheme

To obtain the jets from the final state hadrons, we start by reconstructing jets using the anti-k_T algorithm with a jet radius of $R = 0.5$. After identifying the leading (highest momentum) jet in the transverse momentum region $p_{\text{T}} > p_{\text{T}\text{min}} = 300\,\text{GeV}$ and a pseudo-rapidity in $|\eta_{\text{jet}}| < 1.0$, its constituent particles are reclustered using a generalised-k_T algorithm for some p values and a jet radius of $R = 1.0$. These steps are performed within FastJet v3.3.0 [11].

As previously mentioned, the τ algorithm's clustering measure only coincides with the splitting formation time in the soft and collinear limit, which means not all jets are completely ordered in τ_{form}. Thus, when extracting the formation time of a given splitting, we shall resort to the formula given in the third line of (8) as the working definition of the splitting formation time, for the remainder of this study.

D. Performance of the τ Algorithm

To evaluate the performance of the τ algorithm, we start by considering two proxies for the first splitting formation time: first $\tau_{\text{form}}^{\text{Uncluster}}$, as computed from the substructure properties of reclustered jets, and second, $\tau_{\text{form}}^{\text{PartonShower}}$, as calculated from the kinematic values read from the Monte Carlo event generator, using the third line of (8). The correlation between these variables is plotted in figure 2.

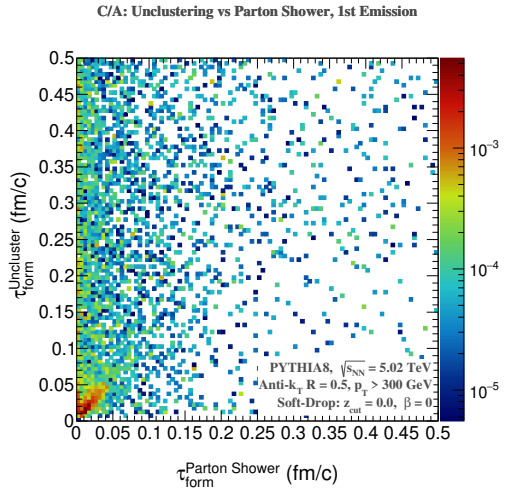

(a) Reclustering with C/A algorithm.

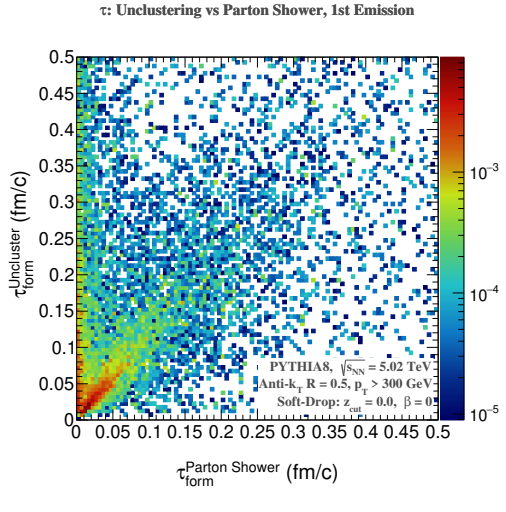

(b) Reclustering with τ algorithm.

FIG. 2: Correlation of τ_{form} between the first parton shower emission and the first unclustering step for different generalised-k$_{\text{T}}$ algorithms.

Both in the case of $p = 0$ (C/A) and $p = 1/2$ (τ), one can see two main features; the diagonal elements, representing true correlations between the reclustering algorithm and the Monte Carlo truth, as well as the vertical band, representing a mismatch between the jet reclustering algorithm and the parton shower values, which can be explained by large angle emissions falling outside the jet cone, leading to uncorrelated emissions.

Although this mismatch can be reduced by increasing the jet radius, this would also increase sensitivity to the underlying event in the case of heavy ion collisions.

Another observation is that the correlation between the reclustered jet and the Monte Carlo history is more pronounced for the τ algorithm. However, given the sensitivity of the C/A algorithm to soft large angle splittings, it is only expected to reproduce the DGLAP kernels when some grooming technique is used. To reduce this sensitivity, we introduce a SoftDrop procedure. Thus, we eliminate all splittings of the leading branch that do not verify the condition

$$z_g \overset{\text{def}}{=} \frac{\min(p_{\text{T1}}, p_{\text{T2}})}{p_{\text{T1}} + p_{\text{T2}}} > z_{\text{cut}} \left(\frac{\Delta R_{12}}{R}\right)^{\beta}. \tag{10}$$

Figure 3 shows the correlation between the τ_{form} variables when the SoftDrop condition with $z_{\text{cut}} = 0.1$ and $\beta = 0$ is enforced. The vertical band at $\tau_{\text{form}}^{\text{PartonShower}} \sim 0$ is greatly reduced for both algorithms, as the relatively soft, large angle emissions falling outside the jet cone have been discarded from both the parton shower and jet histories.

After the application of the jet grooming procedure, the correlation factors have increased from 0.26 to 0.65 for C/A reclustering, and from 0.38 to 0.66 for τ reclustering. As such, SoftDrop grooming is recommended for any jet reconstruction algorithm.

Next, to study how this correlation evolves with the algorithm exponent p, we consider the distribution

$$\Delta\tau_{\text{form}} \overset{\text{def}}{=} \tau_{\text{form}}^{\text{PartonShower}} - \tau_{\text{form}}^{\text{Uncluster}}, \tag{11}$$

of the difference between the proxies for formation time. Thus, a well performing reclustering algorithm is associated with $\Delta\tau_{\text{form}}$ distribution which is both narrow and centred at zero. An example of this distribution can be seen in figure 4, pertaining to C/A reclustered jets.

Due to the skewness and steepness of the $\Delta\tau_{\text{form}}$ distributions, we characterise them by their central value, defined as the median Q_2, and their width, quantified by the first and third quartiles Q_1 and Q_3. This approach allows for quantifying not only the centre and width of the distributions, but also their asymmetry, an important quantity for non-Gaussian distributions.

For PYTHIA8 generated showers, these values were computed for various reclustering algorithm exponents ($p = 0.0; 0.25; 0.5; 0.75; 1.0$) and plotted in figure 5. One observes that, when focusing on the first emission (in orange), all considered algorithms yield $\Delta\tau_{\text{form}}$ distributions centred on zero, with central values of the p exponent producing narrow and symmetric distributions. However, when considering subsequent emissions, the interquartile range (IQR $\overset{\text{def}}{=} Q_3 - Q_1$) becomes significant[1], and exponents of $p \simeq 0.5$ are required to obtain narrow and symmetric distributions.

To evaluate the robustness of these results, we repeated this analysis for JEWEL generated showers without medium effects, which yielded similar results.

[1] This can be understood by noting that $\Delta\tau_{\text{form}}$ increases with τ_{form}, causing the IQR to be larger for the second splitting.

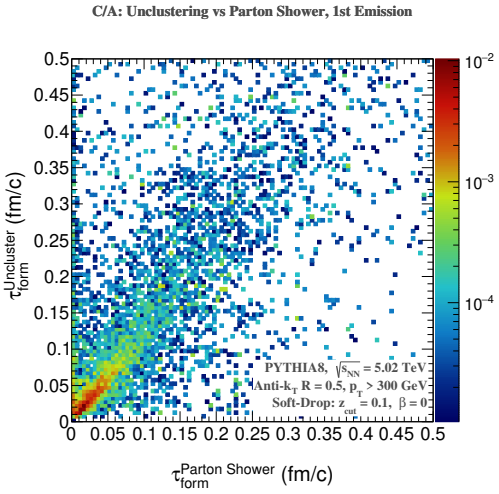

(a) Reclustering with C/A algorithm.

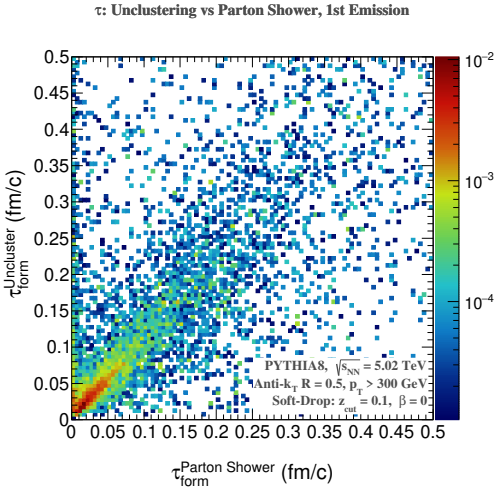

(b) Reclustering with τ algorithm.

FIG. 3: Correlation of τ_{form} between the first parton shower emission and the first unclustering step for different generalised-k_T algorithms with SoftDrop grooming ($z_{\text{cut}} = 0.1$ and $\beta = 0$) in PYTHIA8.

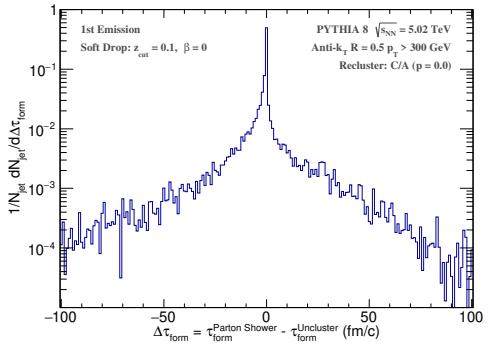

FIG. 4: $\Delta\tau_{\text{form}}$ distribution for the first emission/unclustering step with the C/A jet algorithm ($p = 0$) and $z_{\text{cut}} = 0.1$.

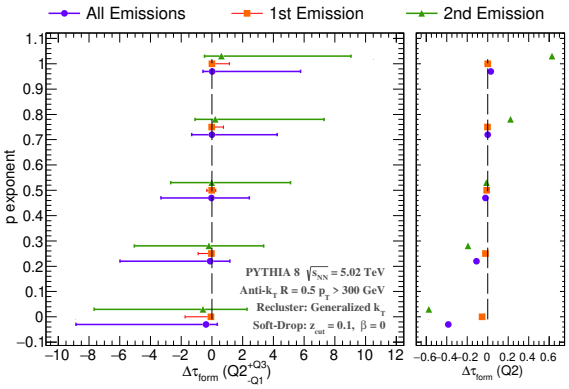

FIG. 5: Median of the $\Delta\tau_{\text{form}}$ distribution obtained for different p values of the algorithms for the first (orange), second (green) or all emissions along the primary branch (purple) in PYHTIA 8 samples. The asymmetric error bars correspond to $+Q_3$ and $-Q_1$ quartiles. The right panel shows a zoom of Q_2 alone.

The values of the median and IQR for the JEWEL samples are similar to those obtained for PYTHIA8 showers, where a value of $p = 0.5$ again yields a centred, symmetric, and narrow distribution. The main differences are found for the second emission, where larger values of p seem compatible with a centred distribution.

Despite the difference in details, central values of the algorithm exponent p appear to yield a better correlation between parton shower and jet histories. In particular, the τ algorithm ($p = 0.5$) shows the best performance with respect to the first emission, especially in providing a symmetric $\Delta\tau_{\text{form}}$ distribution, which is crucial for an unbiased estimation of the formation time.

A similar analysis was performed for medium modified showers, where the algorithms show similar trends. Once again jet grooming proves invaluable in improving the correlation between the unclustering and parton shower formation times.

The $\Delta\tau_{\text{form}}$ distributions are wider than for vacuum-like showers, due to the deterioration of the τ_{form} resolution caused by medium interactions, and to the delaying the first splitting formation time (itself correlated with wider $\Delta\tau_{\text{form}}$ distributions). Despite this, central values of the algorithm exponent $p \sim 0.5$ continue to minimise the median and IQR of the $\Delta\tau_{\text{form}}$ distributions for the medium-modified shower samples, both with and without medium recoils.

E. Jet Quenching Studies

We now turn to an application in heavy ion studies, aiming at a determination of the characteristic timescales for medium evolution. To this end, we start by studying the relevance of the formation time variable in heavy-ion collisions, by plotting the distributions of τ_{form} for JEWEL (pp) and JEWEL (PbPb) showers in figure 6. The clear increase of the average formation time for the first splitting can be explained by medium-induced effects.

For particles participating in the first jet splitting, both elastic and inelastic energy loss are negligible. In the former case, because the incoming parton is highly energetic, and in the latter case because any medium-induced splitting would have a formation time much shorter than the vacuum-like splitting (and thus would be discarded by the JEWEL veto procedure).

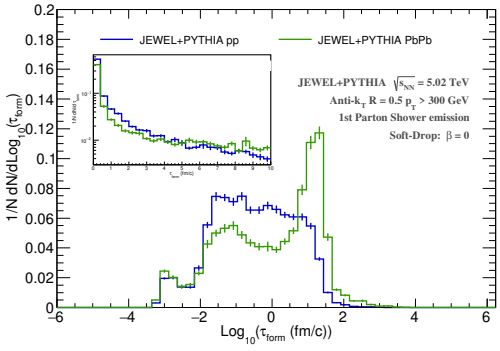

FIG. 6: τ_{form} distribution for the first parton shower emission obtained from JEWEL in pp (blue) and PbPb (green) when using $z_{\text{cut}} = 0.1$. The distribution is shown as a function of $\log_{10}(\tau_{\text{form}})$, and the inset shows the distribution on linear-log scale.

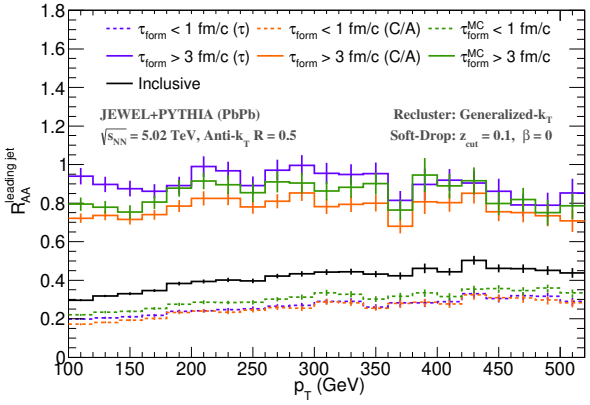

FIG. 7: JEWEL R_{AA} of leading jets. The jets reclustered withτ (C/A) algorithm are shown in purple (orange) when selecting the first groomed unclustering step with $\tau_{\text{form}} > 3\,\text{fm/c}$ ($\tau_{\text{form}} < 1\,\text{fm/c}$) in solid (dashed) lines. We add the results when reading the τ_{form} from the Monte Carlo parton shower in green, and the inclusive spectrum in solid black.

However, jet modification effects also include *jet collimation*, previously found in other observables [12, 13], wherein the surviving jets in PbPb collisions are biased towards a harder fragmentation patters, i.e. hadronise into more energetic final state particles. This increase in transverse momentum biases the jet distributions towards larger formation times (cf. the τ_{form} definition in equation 8). This effect is dominant for the first emission, and explains the shift in the $\log_{10}(\tau_{\text{form}})$ distribution seen in figure 6.

We proceed by computing the nuclear modification factors for the reclustered jets, defined as the ratio between jet yields in medium and in vacuum, which quantifies the jet quenching effects of the medium. This is given by

$$R_{\text{AA}}(p_{\text{T}}) = \frac{N^{\text{pp}}_{\text{evt}}}{N^{\text{AA}}_{\text{evt}}} \frac{\text{d}N^{\text{AA}}_{\text{jet}}/\text{d}p_{\text{T}}}{\text{d}N^{\text{pp}}_{\text{jet}}/\text{d}p_{\text{T}}}\,. \tag{12}$$

We compute the R_{AA} for the leading jets reclustered from JEWEL generated showers, while extending the kinematic region to include lower transverse momentum jets ($p_{\text{T}} > 100\,\text{GeV}$). Using both the Cambridge-Aachen and τ algorithm to recluster the leading jets, we define two different jet populations, according to their formation time; *early jets* with $\tau_{\text{form}} < 1\,\text{fm/c}$, and *late jets* with $\tau_{\text{form}} > 3\,\text{fm/c}$. The $R_{\text{AA}}(p_{\text{T}})$ spectrum of both populations is displayed in figure 7. For reference, the nuclear modification factors obtained from Monte Carlo values have been included (in green), as well as the inclusive spectrum (in black).

By comparing the R_{AA} spectrum of the various populations, we note a clear difference between the jet suppression of the *early* population and that of the full sample. For these jets, C/A and τ results coincide, and are consistent with the interpretation that jets with a fragmentation starting shortly after the hard scattering develop alongside a high density medium, and are therefore strongly modified.

On the other hand, when considering the *late* population the τ algorithm yields an R_{AA} compatible with 1, unlike the C/A algorithm. As discussed above, jets in heavy-ion collisions are biased towards harder fragmentation patterns, and are thus less susceptible to energy loss. We can therefore approximate the *late* jets as a single effective colour charge with high momentum for the first $\sim 3\,\text{fm}$ of its evolution, during which is suffers nearly no energy loss. When this object splits, the medium has diluted considerably (energy density of $\epsilon \sim 5\,\text{GeV/fm}^3$ for the present model and settings), which means that the jet evolves under vacuum-like conditions.

Ultimately, the τ algorithm results are closer to the Monte Carlo values in the previously studied range ($p_{\text{T}} > 300\,\text{GeV}$), which is consistent with the results of the previous sections.

In turn, experimental classification to jet quenching effects at varied and increasingly differential timescales may prove invaluable as tools for precision jet studies, possibly unlocking a tomographic analysis of the QGP at LHC energies.

In this context, the remainder of this work will consist of the first steps towards developing a parton shower ordered in splitting formation time, a choice of ordering variable thus far absent from our studies. To this end, we will begin by examining the emission of two gluons by a high-energy quark in vacuum, placing particular emphasis on the characteristic emission timescales.

III. FACTORISATION OF A DOUBLE GLUON EMISSION

A. Tree Level Amplitude and Eikonal Factor

In Quantum Chromodynamics, in light cone gauge [14, p.1089], the emission of two gluons by an incoming quark has three tree level contributions, listed in figure 8.

Each of the contributions to the process amplitude

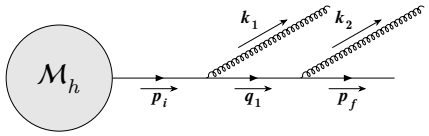

(a) Diagram I — k_1 couples to the 1st vertex.

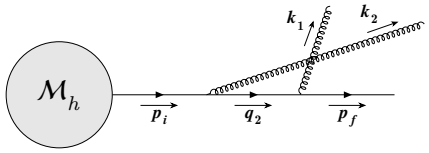

(b) Diagram II — k_1 couples to the 2nd vertex.

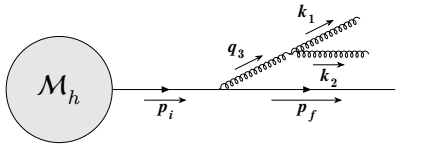

(c) Diagram III — k_1 and k_2 couple to a virtual gluon.

FIG. 8: Contributions for the emission of two gluons by a quark, at tree level, in QCD.

can be written as

$$\begin{aligned}\mathcal{M} = &\int_{p_i,q} (2\pi)^4\delta^{(4)}(q+k_A-p_i)\times\\ &\times(2\pi)^4\delta^{(4)}(k_B+k_C-q)\times\\ &\times\frac{\mathrm{i}}{(p_i^2-m_i^2+\mathrm{i}\,\varepsilon)}\cdot\frac{\mathrm{i}}{(q^2-m_q^2+\mathrm{i}\,\varepsilon)}\times\\ &\times\mathcal{T}(p_i,q)\cdot\mathsf{M}_{\mathrm{h}}(p_i)\,,\end{aligned} \tag{13}$$

where $\mathsf{M}_{\mathrm{h}}(p_i)$ denotes the *hard scattering amplitude*, and contains all the information pertaining to the dynamics of the hard process. On the other hand, the internal four-momentum q as well as the emission part $\mathcal{T}(p_i,q)$ depend on the topology of the successive emissions. The set of four-momenta $\{k_A,k_B,k_C\}$ represent the final state particles, in the arrangement corresponding to a particular diagram.

The emission parts corresponding to each diagram are written

$$\begin{aligned}\mathcal{T}_1 &= \varepsilon_\mu(k_1,\lambda_1)^*\varepsilon_\nu(k_2,\lambda_2)^*\bar{u}(p_f,s_f)\times\\ &\quad\times\ \mathsf{T}^a\,\mathsf{T}^b\,(\mathrm{i}\,g\,\gamma^\nu)\,\not{q}_1\,(\mathrm{i}\,g\,\gamma^\mu)\,\not{p}_i\,,\\ \mathcal{T}_2 &= \varepsilon_\mu(k_1,\lambda_1)^*\varepsilon_\nu(k_2,\lambda_2)^*\bar{u}(p_f,s_f)\times\\ &\quad\times\ \mathsf{T}^b\mathsf{T}^a(\mathrm{i}\,g\,\gamma^\mu)\,\not{q}_2\,(\mathrm{i}\,g\,\gamma^\nu)\,\not{p}_i\,,\\ \mathcal{T}_3 &= \varepsilon_\mu(k_1,\lambda_1)^*\varepsilon_\nu(k_2,\lambda_2)^*\bar{u}(p_f,s_f)\times\\ &\times\ f^{abc}\mathsf{T}^c(\mathrm{i}g\gamma^\sigma)S_{\sigma\rho}(q_3)\,g\Gamma^{\rho\mu\nu}(q_3,-k_1,-k_2)\,\not{p}_i\,,\end{aligned} \tag{14}$$

in accordance with the QCD Feynman rules in light cone gauge.

After performing a Fourier transform in the p^- momentum components and integrating over the propagator poles, the amplitude contributions are shown to have the form

$$\begin{aligned}\mathcal{M} = \int_{x_0^+<x_1^+<x_2^+} &\frac{\mathrm{e}^{\,\mathrm{i}\,x_0^+\frac{|\boldsymbol{p}_{\perp i}|^2}{2\,p_i^+}}}{2\,p_i^+\cdot 2\,q^+}\times\\ &\times\ \mathrm{e}^{\,\mathrm{i}\,\frac{x_1^+}{t_{\mathrm{f}}(p_i\to q,k_A)}}\,\mathrm{e}^{\,\mathrm{i}\,\frac{x_2^+}{t_{\mathrm{f}}(q\to k_B,k_C)}}\times\\ &\times\ \mathcal{T}^{\mathrm{on-shell}}(p_i,q)\cdot\mathsf{M}_{\mathrm{h}}(x_0^+)\,,\end{aligned} \tag{15}$$

where $x_{1,2}^+$ are the light cone times associated with each emission. These times present with a characteristic phase, identified as

$$t_{\mathrm{f}}(p\to p_1,p_2)^{-1} = \frac{p^+}{2}z(1-z)\left|\frac{\boldsymbol{p}_{\perp 1}}{p_1^+}-\frac{\boldsymbol{p}_{\perp 2}}{p_2^+}\right|^2, \tag{16}$$

with z as the light cone momentum fraction of the daughters, and $\boldsymbol{p}_{\perp i}$ their transverse momentum.

In the context of the diagonal contributions to $|\mathcal{M}|^2$, by writing the $\mathcal{M}^*$ integrations over $\bar{x}_{1,2}$, we find

$$\begin{aligned}\mathcal{M}\,\mathcal{M}^* \propto &\int_{x_1^+,\bar{x}_1^+}\exp\left\{\mathrm{i}\frac{(x_1^+-\bar{x}_1^+)}{t_{\mathrm{f}}(p_i\to k_A,q)}\right\}\times\\ &\times\int_{x_2^+,\bar{x}_2^+}\exp\left\{\mathrm{i}\frac{(x_2^+-\bar{x}_2^+)}{t_{\mathrm{f}}(q\to k_B,k_C)}\right\}.\end{aligned} \tag{17}$$

We identify the differences $x_j^+-\bar{x}_j^+$ as the uncertainties in the light cone times for both splittings, and note how they oscillate with characteristic timescales given by the phases $t_{\mathrm{f}}(p\to p_1,p_2)$. These are therefore identified as the *splitting formation times*, and in the soft limit for gluon emission reduce to

$$t_{\mathrm{f},j}^{-1}\propto k_j^+\theta_j^2 = p^+ z_j\,\theta_j^2\,, \tag{18}$$

for the formation time of gluon j. Further, the angular ordering prescriptions can be rewritten as an ordering in formation times,

$$\theta_1\gg\theta_2\iff t_{\mathrm{f}1}^{-1}\gg t_{\mathrm{f}2}^{-1}\,, \tag{19}$$

valid in the soft regime, outside of which finite energy correction become important, as seen in the previous section.

B. Suppression of the Interference Terms

Because this interpretation for the splitting formation times is only valid in the context of the diagonal contributions to $|\mathcal{M}|^2$, we must compute all contributions to verify that the interference terms do not show any enhancement. This is visible in the colour suppression of the interference between the first two diagrams.

From (14), we can read the colour factors correspond-

ing to each diagram

$$\begin{aligned}\mathsf{G}_1^{ab} &= (-1)\ \mathsf{T}^a\,\mathsf{T}^b\,,\\ \mathsf{G}_2^{ab} &= (-1)\ \mathsf{T}^b\,\mathsf{T}^a\,,\\ \mathsf{G}_3^{ab} &= \mathrm{i}\ f^{abc}\,\mathsf{T}^c\,,\end{aligned} \tag{20}$$

Define the colour factors as the sum over adjoint and fundamental indices, divided by the number of possible colours of the initial quark,

$$\mathcal{K}_{XY} \stackrel{\text{def}}{=} \frac{1}{N}\sum_{i,j}\sum_{a,b}(\mathsf{G}_Y^*)_{ij}^{ab}(\mathsf{G}_X)_{ij}^{ab}\,. \tag{21}$$

Using the SU(N) group algebra and the definitions $C_A = N$ and $C_F = \frac{N^2-1}{2\,N}$, these are written

$$\begin{aligned}\mathcal{K}_{11} &= C_F^2 = \mathcal{O}(N^2)\,,\\ \mathcal{K}_{22} &= C_F^2 = \mathcal{O}(N^2)\,,\\ \mathcal{K}_{33} &= C_F C_A = \mathcal{O}(N^2)\\ \mathcal{K}_{12} &= \mathcal{K}_{21} = -\frac{C_F}{2\,N} = \mathcal{O}(1)\,,\\ \mathcal{K}_{13} &= \mathcal{K}_{31} = -\frac{N\,C_F}{2} = \mathcal{O}(N^2)\,,\\ \mathcal{K}_{23} &= \mathcal{K}_{32} = +\frac{N\,C_F}{2} = \mathcal{O}(N^2)\,.\end{aligned} \tag{22}$$

showing the colour suppression of the interference term $\mathcal{K}_{12}$. Despite not being colour suppressed, the other interference terms can be included in the diagonal contributions.

When looking at the Dirac structure, no enhancement of the interference terms is found, and the diagonal terms show the factorisation of the splitting kernels for each emission, in the soft limit for the gluons. With this result in hand, we move towards considering multiple gluon radiation by a quark, in the context of a parton shower.

IV. ORDERING VARIABLES FOR PARTON SHOWERS

Next, we aim to study the dynamics of parton shower cascades by implementing parton showers according to the *double logarithm approximation* (DLA). For simplicity, we focus on multiple gluon emissions by a single quark, as ordered according to their virtual mass, transverse momentum, and angle.

A. The Double Logarithm Approximation

By evaluating the QCD coupling constant at some fixed scale $\alpha(\mu^2) \longrightarrow \alpha(m_Z^2)$, and approximating the DGLAP splitting kernels as

$$\begin{aligned}\sum_i \hat{P}_{i\leftarrow q}(z) &\simeq \frac{2\,C_F}{z}\,,\\ \sum_i \hat{P}_{i\leftarrow g}(z) &\simeq \frac{2\,C_A}{z}\,,\end{aligned} \tag{23}$$

the integrand of the Sudakov form factor as given by (4) becomes doubly logarithmic. This captures the basic features of parton cascades in the soft collinear limit, and can be used for a probabilistic sampling of parton emissions.

This is done by inversion sampling, wherein the range $[0,1]$ of the Sudakov factor is sampled uniformly, by setting it equal to a random number,

$$\Delta_a(Q^2_{\text{max}}, Q^2) = \mathcal{R}\,, \tag{24}$$

yielding a condition which can then be inverted, sampling the scale of the next emission Q^2 correctly. The same can be done to sample the fractions z, taken as the light cone fractions of the splittings, by using the cumulative distribution of the splitting kernels,

$$F(z_n) \stackrel{\text{def}}{=} \frac{\int_{z_{\text{min}}}^{z_n} \mathrm{d}u/u}{\int_{z_{\text{min}}}^{1-z_{\text{min}}} \mathrm{d}u/u} = \frac{\ln(z_n/z_{\text{min}})}{\ln(1/z_{\text{min}}-1)}\,, \tag{25}$$

where the kinematic limit z_{min} is determined from momentum conservation.

In line with our aim to study the differences between various ordering prescriptions, we adopt the approach of choosing some ordering variable $\mu_n^2 = p_n^2 f(z_n)$, where p_n^2 is the virtual mass of the mother. In this thesis, we focus on the following choices for μ_n^2

$$\begin{aligned}&p_n^2\,, && \text{the mother's virtual mass.}\\ &\tilde{\boldsymbol{p}}_{\perp n}^2 \stackrel{\text{def}}{=} z_n(1-z_n)\,p_n^2\,, && \text{the transverse momentum.}\\ &\zeta_n \stackrel{\text{def}}{=} \frac{p_n^2}{z_n(1-z_n)}\,, && \text{the splitting angle.}\end{aligned} \tag{26}$$

Our implementation clearly differs between ordering prescriptions, because the same (μ_n^2, z_n) pair would produce different virtual masses, therefore requiring different kinematic limits on the light cone fraction, denoted by z_{min} and z_{max}.

After obtaining the kinematic limits for each ordering prescription and evaluating the double integral in the Sudakov form factor given by (4), we can proceed with sampling the parton emissions for all prescriptions.

For the three ordering prescriptions under study, condition (24) is

$$\begin{aligned}\frac{p_n^2}{Q^2_{\text{had}}} &= \exp\left\{+\sqrt{\ln^2\frac{p^2_{n,\text{max}}}{Q^2_{\text{had}}} + \frac{1}{\bar{\alpha}}\ln\mathcal{R}_\Delta}\right\},\\ \frac{\tilde{\boldsymbol{p}}_{\perp n}^2}{p^2_{n,\text{max}}} &= \exp\left\{-\sqrt{\ln^2\frac{\tilde{\boldsymbol{p}}^2_{\perp n-1}}{p^2_{n,\text{max}}} - \frac{1}{\bar{\alpha}}\ln\mathcal{R}_\Delta}\right\},\\ \frac{\zeta_n}{Q^2_{\text{had}}} &= \exp\left\{+\sqrt{\ln^2\frac{\zeta_{n-1}}{Q^2_{\text{had}}} + \frac{2}{\bar{\alpha}}\ln\mathcal{R}_\Delta}\right\},\end{aligned} \tag{27}$$

for quark initiated splittings[2], where $p^2_{n,\text{max}} \stackrel{\text{def}}{=} p^2_{n-1}z_{n-1}$.

[2]The first splitting requires slightly different limits, as the up-

To sample the light cone fractions, an equivalent method is employed, using the cumulative distribution defined in (25). This has the form $F(z_n) = \mathcal{R}_z$, written as

$$z_n = z_{\min}(\mu_n^2) \cdot \left(\frac{1}{z_{\min}(\mu_n^2)} - 1\right)^{\mathcal{R}_z}, \tag{28}$$

where $z_{\min}(\mu_n^2)$ corresponds to

$$\begin{aligned} z_{\min} &= \frac{Q_{\text{had}}^2}{p_n^2}, \text{ for } p_n^2 \text{ ordering,} \\ z_{\min} &= \frac{\tilde{\boldsymbol{p}}_{\perp n}^2}{p_{n,\max}^2}, \text{ for } \tilde{\boldsymbol{p}}_{\perp n}^2 \text{ ordering,} \\ z_{\min} &= \sqrt{\frac{Q_{\text{had}}^2}{\zeta_n}}, \text{ for } \zeta_n \text{ ordering.} \end{aligned} \tag{29}$$

This procedure generates a (μ_n^2, z_n) such that $z_n \in [z_{\min}(\mu_n^2), 1 - z_{\min}(\mu_n^2)]$. However, the kinematically allowed phase space is more restrictive than this condition. To overcome this difficulty, $(\mu_{n,\text{trial}}^2, z_{n,\text{trial}})$ pairs sampled according to this procedure which do not obey the full kinematic restrictions are ignored and resampled, starting from the the trial scale $\mu_{n,\text{trial}}^2$.

This procedure starts at some scale Q_{coll}^2 set by the hard scattering, and continues until the available phase space for parton splittings vanishes, near some hadronisation scale Q_{had}^2.

B. Results

Here, we present some results pertaining to the parton showers we have implemented based on the previous section. The hard scattering sets the upper bound for the virtual mass of the first quark, $Q_{\text{coll}}^2 = 1\,\text{TeV}^2$, and the initial parton was given a momentum of $|\boldsymbol{p}| = p_{z,\text{init}} = 10\,\text{TeV}$, such that it is ultra-relativistic. The hadronisation scale is set at $Q_{\text{had}}^2 = 1\,\text{GeV}^2$.

For the angular ordered shower, the initial variable was limited at $\zeta_0 = (p_z\pi)^2$, effectively vetoing the upper bound on the first emission. For each prescription 10^6 events were generated according to the algorithms described in the previous sections.

1. Kinematic Distributions

We start by looking at the distribution of the number of emissions for each of the three prescriptions, depicted in figure 9. Although all distributions are peaked at $N_g = 4$, the angular and transverse momentum ordered showers show a significant suppression of gluon emissions. This is explained by noting that these prescriptions implement coherence effects which are not fully present in the virtuality ordering prescription.

To understand quark energy loss due to gluon radiation, we look at the quark's energy distributions before splittings 2, 3, and 4, for an angular ordered shower,

per bound for the virtual mass of the first quark is set by the hard scattering.

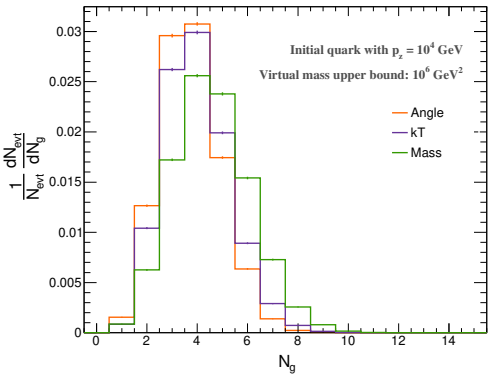

FIG. 9: Number of emissions undergone by the quark for each ordering prescription.

as depicted in figure 10. We find that all distributions begin peaked at $p_{z,\text{init}} = 10\,\text{TeV}$, flattening as one advances along the shower.

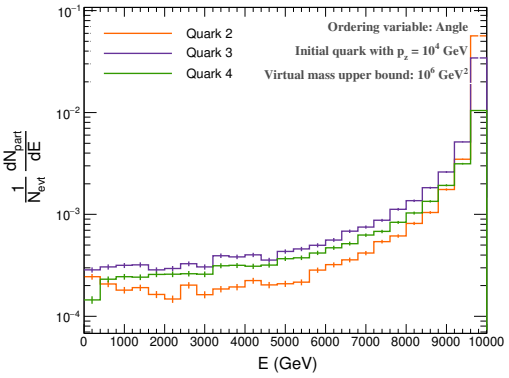

FIG. 10: Energy distribution of quarks 2 — 4 (i.e. after splittings 1 — 3).

2. The Lund Plane

The different behaviours of the ordering prescriptions are best examined with recourse to the Lund plane [15, 16] distributions of each splitting. These are usually given in the $(\ln(1/\theta), \ln(1/z_E))$ plane, where z_E is the gluon energy fraction with respect to the quark, and θ is the angle between the daughters' three momenta.

Besides this configuration, we explore the $\big(\log_{10}(\tau_{\text{form}}), \log_{10}(\pi/\theta)\big)$ plane, where τ_{form} corresponds to the splitting formation time as given by the third line of (8). In this configuration of the Lund plane and for angular ordered showers, the distributions of the first four splittings are shown in figure 11.

The Lund plane evolution of the angular ordered parton cascades is characterised by a shift towards narrower splitting angles, as a consequence of the coherence effects described above, and towards larger values of τ_{form}, corroborating the use of this variable as a splitting formation time.

In general, the other prescriptions show a similar (yet not identical) trend in their evolution, differing in the specifics of the initial distributions.

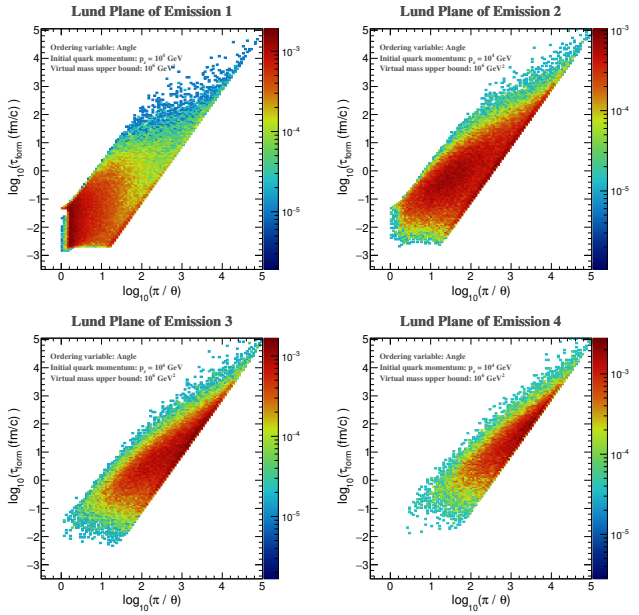

FIG. 11: Lund plane in $\log_{10}(\tau_{\text{form}})$ vs $\log_{10}(\pi/\theta)$ for the first four emissions of a parton shower ordered according to splitting angle.

To better examine the evolution of the Lund plane distributions, we compute the mean value of each kinematic value, τ_{form}, and θ for each splitting, and show the path traced over the Lund plane by each ordering prescription in figure 12.

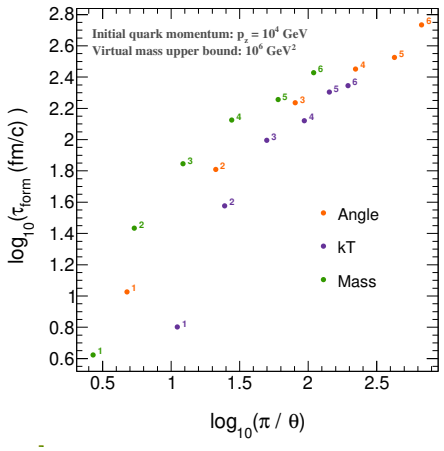

FIG. 12: Path traced the three algorithms, given by the mean values for the $\log_{10}(\tau_{\text{form}})$ vs $\log_{10}(\pi/\theta)$ Lund plane variables.

On the other hand, figure 12 shows the trajectories in the $\big(\log_{10}(\pi/\theta), \log_{10}(\tau_{\text{form}})\big)$ plane, evolving towards narrower splitting angles and larger values of formation time.

The general decrease of splitting angle once again emphasises the coherence effects observed throughout this section and motivated by the angular ordering results for a QCD antenna.

There is, however, significant variation between the trajectories of different ordering prescriptions, highlighting the need for theoretical control of the parton shower kinematics, beyond DLA accuracy.

V. CONCLUSIONS

In this work, the characteristic timescales for QCD emissions were studied, with the ultimate aim to implement a parton shower ordered according to the formation time of the parton splittings.

First, we have studied a new jet reclustering tool, the τ algorithm, whose distance measure coincides with the inverse splitting formation time τ_{form} in the soft limit. This jet clustering algorithm is obtained by choosing $p = 1/2$ for the generalised-k_T distance measure, such that it clusters jets in τ_{form}^{-1} To study the performance of this novel jet reclustering algorithm, we use parton showers with different ordering variables. When compared to C/A algorithm, we found the τ algorithm to provide jets better correlated with the parton shower Monte Carlo truth. It also produced better estimates for τ_{form} than C/A, although jet grooming proved essential in this task. In the context of jet quenching studies, the τ algorithm was found to produce jets with a first splitting formation time such that the *late* population does not undergo significant modifications, unlike the C/A algorithm, which systematically underestimates τ_{form}.

As these results show the importance of parton shower ordered in formation time, an ordering thus far missing from our study. To achieve this goal, we examined the calculation of the amplitude for double gluon emission from a quark, aiming to compute τ_{form} from an analytical expression and to verify factorisation into single gluon emissions. This was done by writing the contributions of all tree level diagrams in terms of their Dirac and colour structure, and an eikonal factor. From this, the characteristic timescales of each gluon emission were identified, in the context of the diagonal terms in $|\mathcal{M}|^2$. In the soft limit, these timescales were shown to coincide with the definition of formation time used for heavy ion studies in previous sections. Further, formation time ordering can recovered from the angular ordering prescription in the soft limit, as given by pQCD calculations. In examining the $|\mathcal{M}|^2$ contributions, the off-diagonal terms were found to be either colour suppressed or possible to include as contributions to the diagonal terms, which were shown to factorise into the splitting kernels for successive gluon emissions, in the soft limit.

Finally, the working principles of a parton shower in the DLA regime were explored for the three most common ordering variables namely virtuality, transverse momentum, and splitting angle. By implementing the appropriate kinematic restrictions in all cases, the four-momenta of all participating partons were reconstructed, allowing for comparisons between prescriptions. Next, the Lund plane distributions were studied for all three prescriptions, where the variation between the ordering prescriptions was observed, due to their dynamics and starting configurations. This is also manifest in the trajectories over the Lund planes, with significant differences in values τ_{form} which, while within DLA accuracy, may prove crucial in heavy ion studies, due to the short timescale for QGP evolution.

[1] R. K. Ellis, W. J. Stirling, and B. R. Webber, *QCD and collider physics*, Cambridge monographs on particle physics, nuclear physics, and cosmology (Cambridge University Press, Cambridge, 2003) photography by S. Vascotto.

[2] Y. L. Dokshitzer, V. A. Khoze, A. H. Mueller, and S. I. Troian, *Basics of perturbative QCD* (Editions Frontiers, 1991) p. 10.

[3] J. J. Ethier and E. R. Nocera, Annual Review of Nuclear and Particle Science **70**, 43 (2020), arXiv: 2001.07722.

[4] A. Metz and A. Vossen, Progress in Particle and Nuclear Physics **91**, 136–202 (2016).

[5] L. Apolinário, J. G. Milhano, G. P. Salam, and C. A. Salgado, Physical Review Letters **120**, 10.1103/physrevlett.120.232301 (2018).

[6] J. Casalderrey-Solana and E. Iancu, Journal of High Energy Physics **2011**, 10.1007/jhep08(2011)015 (2011).

[7] J. Casalderrey-Solana, Y. Mehtar-Tani, C. A. Salgado, and K. Tywoniuk, Physics Letters B **725**, 357 (2013).

[8] L. Apolinário, A. Cordeiro, and K. Zapp, The European Physical Journal C **81**, 10.1140/epjc/s10052-021-09346-8 (2021).

[9] T. Sjöstrand, S. Mrenna, and P. Skands, Computer Physics Communications **178**, 852 (2008).

[10] K. C. Zapp, The European Physical Journal C **74**, 2762 (2014), arXiv: 1311.0048.

[11] M. Cacciari, G. P. Salam, and G. Soyez, Eur. Phys. J. C **72**, 1896 (2012), arXiv:1111.6097 [hep-ph].

[12] J. Casalderrey-Solana, J. G. Milhano, and U. A. Wiedemann, Journal of Physics G: Nuclear and Particle Physics **38**, 035006 (2011).

[13] L. Apolinário, J. G. Milhano, M. Ploskon, and X. Zhang, The European Physical Journal C **78**, 10.1140/epjc/s10052-018-5999-2 (2018).

[14] G. Leibbrandt, Reviews of Modern Physics **59**, 1067 (1987).

[15] F. A. Dreyer, G. P. Salam, and G. Soyez, JHEP **12**, 064, arXiv:1807.04758 [hep-ph].

[16] H. A. Andrews *et al.*, J. Phys. G **47**, 065102 (2020), arXiv:1808.03689 [hep-ph].